



## Size-dependent nanoconfinement effects in magnesium hydride

Lijun Fang<sup>a,b</sup>, ChenKai Liu<sup>a,b</sup>, Yonghong Feng<sup>a,b</sup>, Zefan Gao<sup>a,b</sup>, Shilong Chen<sup>a,b</sup>,  
Mingye Huang<sup>a,b</sup>, Han Ge<sup>a,b</sup>, Linbin Huang<sup>c</sup>, Zhengyang Gao<sup>a,b</sup>, Weijie Yang<sup>a,b,\*</sup>

<sup>a</sup> Department of Power Engineering, School of Energy, Power and Mechanical Engineering, North China Electric Power University, Baoding, 071003, China

<sup>b</sup> Hebei Key Laboratory of Low Carbon and High Efficiency Power Generation Technology, North China Electric Power University, Baoding, 071003, Hebei, China

<sup>c</sup> Guoneng Nanjing Electric Power Test & Research Limited, Jiangsu, China

### ARTICLE INFO

Handling Editor: Prof. A.B. Basile

#### Keywords:

MgH<sub>2</sub>  
Particle size/pore size  
Charge transfer  
Nanoconfinement  
DFT calculation

### ABSTRACT

Nanoconfinement effect is crucial to improve the dehydrogenation kinetics of MgH<sub>2</sub>. However, the underlying micro-mechanism for nanoconfinement effect of carbon-based carrier on MgH<sub>2</sub> nanoparticles is still ambiguous, hindering the design of carbon-based nanoconfined MgH<sub>2</sub> nanoparticles. To address this dilemma, we applied density functional theory (DFT) calculations to investigate the interaction between carbon-based carrier and MgH<sub>2</sub> nanoparticles. To analyze this issue, we designed various systems of carbon nanotubes nanoconfined MgH<sub>2</sub> nanoparticles, with the range of particle size/pore size ratio from 0.3 to 0.8. The interaction strength between carbon-based carrier and MgH<sub>2</sub> nanoparticles gradually increases with the increase of particle size/pore size ratio, and the dehydrogenation temperature decreases with the increase of particle size/pore size ratio. The electron of carbon-based carrier will transfer to MgH<sub>2</sub> nanoparticles, leading to the weakening of Mg–H bonds. The weakened Mg–H bonds corresponding to lower dehydrogenation barrier, which is consistent with the phenomenon that the dehydrogenation temperature is inversely proportional to particle size/pore size ratio in calculations and experiments. This work not only elucidates the size-dependent nanoconfinement effects on MgH<sub>2</sub> from a microscopic perspective, but also provides the theoretical basis for the design and development of carbon-based nanoconfined MgH<sub>2</sub> nanoparticles.

### 1. Introduction

Hydrogen energy, as a clean and efficient alternative, has garnered considerable attention [1–3]. Solid-state hydrogen storage [4,5], renowned for its high density, safety, and stability, exhibits promising applications [6]. However, obstacles such as slow hydrogen absorption rate, increased storage temperature, and high cost have impeded its widespread adoption and application in practical settings [7–9]. Therefore, safe and efficient hydrogen storage and transportation have emerged as paramount research priorities [10,11]. Among solid-state materials, magnesium hydride (MgH<sub>2</sub>) [12] has high theoretical storage capacity, excellent reversibility, and high hydrogen storage density (7.69 wt%) [6,13]. However, its high dehydrogenation temperature (>300 °C) [14,15] and slow hydrogen storage kinetics [16,17] severely hinder its commercialization process.

Therefore, strategies such as nanostructures [18–21] and spatial nanoconfinement [22–25] have been proposed to regulate and optimize

the hydrogen storage and release kinetics [19] and thermodynamics [26] of MgH<sub>2</sub>. Wu et al. [27] examined the nanoconfinement of MgH<sub>2</sub> (5.9–15.7 nm) in CNTs (9.5–34.9 nm), achieving 1–20 wt% confinement. They found that as the MgH<sub>2</sub>/CNT pore diameter ratio rose from 0.41 to 0.61, the initial dehydrogenation temp. dropped significantly from 369 °C to 337 °C. Similarly, Priscilla Huen et al. [28] confined MgH<sub>2</sub> in carbon aerogels (CAs), observing a decrease in initial dehydrogenation temp. from 250 °C to 210 °C as the particle-to-pore ratio rose from 0.52 to 0.77. Research by Yuen S. Au et al. [29] similarly reported a drop from 275 °C to 253 °C with increasing ratio in carbon aerogels. Additionally, Jia et al. [30] found in CMK-3 that as the ratio decreased from 0.5 to 0.18, the temp. fell from 152 °C to 102 °C. Notably, Zlotea et al. [31] achieved a remarkably low 117 °C with CT carbon with particle-to-pore diameters close to 1.3 nm. Zhang et al. [32] examined the impact of element-doped graphene (B, N, Si, P, S, Fe, Co, Ni, Al) on MgH<sub>2</sub> dehydrogenation enthalpies. Notably, B-doped graphene significantly outperformed other modifications in catalyzing Mg<sub>4</sub>H<sub>8</sub>/Mg<sub>6</sub>H<sub>12</sub> clusters.

\* Corresponding author. Department of Power Engineering, School of Energy, Power and Mechanical Engineering, North China Electric Power University, Baoding, 071003, China.

E-mail address: [yangwj@ncepu.edu.cn](mailto:yangwj@ncepu.edu.cn) (W. Yang).

<https://doi.org/10.1016/j.ijhydene.2024.11.233>

Received 25 September 2024; Received in revised form 7 November 2024; Accepted 13 November 2024

0360-3199/© 2024 Hydrogen Energy Publications LLC. Published by Elsevier Ltd. All rights are reserved, including those for text and data mining, AI training, and similar technologies.

The  $\text{MgH}_2+5$  wt% CNTs composites prepared by Xu et al. [33] maintained a stable capacity of 6.3 wt% in 10 cycles without significant degradation.  $\text{MgH}_2@$ B/CNTs delivers a high reversible capacity of 5.78 wt% (equivalent to up to 99.8% of the original capacity) was maintained after 10 cycles with no significant degradation of the dynamics [34]. However, the enhancement of  $\text{MgH}_2$  dehydrogenation and cycling stability by carbon carriers in the literature is limited. The reason for this deficiency may be our insufficient understanding of the mechanism of  $\text{MgH}_2$  dehydrogenation limited by carbon carriers.

Therefore, in order to study the mechanism, corresponding research work should be carried out in both experiments and theoretical calculations. However, there are still two challenges to be faced. In-situ characterization of CNT-nanoconfined  $\text{MgH}_2$  faces challenges like nanoscale complexity, capturing rapid dynamic hydrogen absorption/desorption, environmental influences, and sample prep difficulties. Ensuring  $\text{MgH}_2$  uniformity, controlling morphology/composition, and minimizing impurities/defects are vital. Advancements in characterization technology will likely overcome these challenges, bolstering  $\text{MgH}_2$  solid-state hydrogen storage research. DFT calculations for CNT-nanoconfined  $\text{MgH}_2$  hydrogen storage face complexities: intricate CNT- $\text{MgH}_2$  interactions, diverse bonding types, and morphological factors affecting  $\text{MgH}_2$  distribution. Large systems with numerous atoms amplify computational demands, requiring balance between accuracy and efficiency. Overcoming these challenges necessitates advanced computing methods and substantial resources.

In this work, we focus on the hydrogen storage and release kinetics and cycling stability of carbon constrained  $\text{MgH}_2$  nanoparticles. We delved into the effects of CNTs with different pore sizes on the hydrogen storage and release performance of  $\text{MgH}_2$  clusters, and sought to enhance dehydrogenation ability through B-doped carbon-based carriers. We reveal the anchoring effect of CNTs on  $\text{MgH}_2$  nanoparticles and the activation mechanism of H–Mg bonds based on their structural characteristics and H–Mg bond properties. We also investigated the effect of initial dehydrogenation temperature on carbon nanotube confined  $\text{MgH}_2$  cluster systems with different particle size to pore size ratios under different pressures. Meanwhile, we study the charge transfer characteristics between non-uniform interfaces and explore the size matching mechanism between the pore size of CNTs and the particle size of  $\text{MgH}_2$  nanoparticles. Ultimately, we expect to develop a regulatory strategy to synergistically optimize the thermodynamic, kinetic, and cyclic stability of  $\text{MgH}_2$  solid-state hydrogen storage materials. Through a detailed study of the size matching effect between CNTs and  $\text{MgH}_2$  nanoparticles, we aim to provide a solid theoretical basis and experimental support for the commercial application of solid-state hydrogen storage technology.

## 2. Method

In this study, calculations were performed using the ORCA 5.0.3 package based on Density Functional Theory (DFT) [35,36]. VMD [37] software was employed for visualization and result plotting. The structural optimization and frequency analysis were conducted using the PBE0-D3 functional combined with the def2-TZVP(-f) basis set (including DFT-D3). Single-point energy calculations were performed using the B3LYP-D3 hybrid functional with the def2-TZVP(-f) basis set (including DFT-D3), which has been proven to be an accurate method for small organic systems. Optimizing hybrid functionals, especially vibration analysis, is very expensive. Optimization and vibration analysis are much less sensitive to computational levels than energy calculations. The use of ordinary functionals such as PBE0-D3 in structural optimization and vibration analysis can effectively save time and computational costs, while the use of hybrid functionals such as B3LYP-D3 in single point energy calculations can ensure better accuracy. To accelerate the calculations, the RIJCOX method was used [38].

The CNT structures used were constructed in Materials Studio and Avogadro software [39,40], where periodicity was eliminated, and

hydrogenation was performed at the entrance and exit positions of the CNTs. The  $(\text{MgH}_2)_n$  nanoparticle clusters were initially generated using the Molclus program [41] combined with the MOPAC program, utilizing the PM6 functional, to produce the 10 lowest-energy configurations of  $(\text{MgH}_2)_n$  ( $n = 1-9$ ) nanoclusters from 200 candidate structures. The spin multiplicity for both CNTs and  $\text{MgH}_2$  is designated as 1. The final structure with the lowest energy was selected after geometric optimization and single-point energy calculations using the B3LYP hybrid functional combined with the def2-TZVP(-f) basis set (including DFT-D3). Among them, the original  $\text{MgH}_2$  clusters generated by Molclus are displayed in the  $\text{MgnH}_2n.\text{xyz}$  ( $n = 1-9$ ) file. The formation energy of  $\text{MgH}_2$  clusters was calculated using the following equation (1):

$$E_F = E((\text{MgH}_2)_n) - nE(\text{Mg}) - nE(\text{H}_2) \quad (1)$$

where  $E_F$  is the formation energy [42] of the  $\text{MgH}_2$  nanocluster,  $E((\text{MgH}_2)_n)$  is the total energy of the  $\text{MgH}_2$  nanocluster,  $E(\text{Mg})$  is the energy of a single Mg atom, and  $E(\text{H}_2)$  is the energy of  $\text{H}_2$ .

To further investigate the anti-aggregation or nanoconfinement effect of pristine/modified CNTs on  $\text{MgH}_2$  nanoparticles, the binding energy  $E_B$  between the  $(\text{MgH}_2)_n$  cluster (structure A) and the pristine/modified CNT (structure B) was calculated using equations (2)–(4):

$$E_B = E(AB) - E(A) - E(B) + E_{BSSE} \quad (2)$$

$$E_{BSSE} = (E(A) - E_{AB}(A)) + (E(B) - E_{AB}(B)) \quad (3)$$

$$E_B = E(AB) - E_{AB}(A) - E_{AB}(B) \quad (4)$$

Where  $E(AB)$  is the total energy of the  $\text{MgH}_2$  nanoparticle nanoconfined within the pristine/modified CNT,  $E(A)$  is the energy of the  $(\text{MgH}_2)_n$  cluster nanoparticle,  $E(B)$  is the energy of the pristine/modified CNT,  $E_{AB}(A)$  is the energy of the  $(\text{MgH}_2)_n$  cluster nanoparticle corrected for basis set superposition error (BSSE), and  $E_{AB}(B)$  is the energy of the pristine/modified CNT corrected for BSSE.

To further demonstrate the influence of different particle-to-pore size ratios on the dehydrogenation performance of  $(\text{MgH}_2)_n$  nanoparticles nanoconfined within CNTs, the bond length of Mg–H bonds, Mayer bond order, charge density difference maps, and ELF [43,44] maps were analyzed using the Multiwfn [41] wave function analysis program developed by Lu Tian [45], based on the analysis of molden wave function files.

The Mayer level [46] between atom A and B is defined as

$$I_{AB} = I_{AB}^\alpha + I_{AB}^\beta = 2 \sum_{a \in A} \sum_{b \in B} [(P^\alpha S)_{ba} (P^\alpha S)_{ab} + (P^\beta S)_{ba} (P^\beta S)_{ab}] \quad (5)$$

where  $P^\alpha$  and  $P^\beta$  are alpha and beta density matrix respectively,  $S$  is overlap matrix. Above formula can be equivalently rewritten using total density matrix  $P = P^\alpha + P^\beta$  and spin density matrix  $P^S = P^\alpha - P^\beta$ .

$$I_{AB} = \sum_{a \in A} \sum_{b \in B} [(PS)_{ba} (PS)_{ab} + (P^S S)_{ba} (P^S S)_{ab}] \quad (6)$$

For restricted closed-shell circumstance, since spin density matrix is zero, the formula can be simplified to

$$I_{AB} = \sum_{a \in A} \sum_{b \in B} (PS)_{ab} (PS)_{ba} \quad (7)$$

Generally, the value of Mayer level is in agreement with empirical bond order; for single, double and triple bonds, the values are close to 1.0, 2.0 and 3.0 respectively. For unrestricted or restricted open-shell wavefunction, alpha, beta and total Mayer level will be outputted separately. From a physical perspective, the Mayer level serves as an indicator of the number of electrons shared between two atoms. For comparable chemical bonds, a positive correlation exists between the Mayer level and bond strength. In this study, only those Mayer levels exceeding 0.05 will be deemed valid and incorporated into the subsequent calculations.

The charge transfer amounts in this article were calculated using the charge model 5(CM5) [45,47] method, yields class IV partial atomic charges by mapping from those obtained by Hirshfeld [48] population analysis of density functional electronic charge distributions. the expression of CM5 charge is:

$$q_i^{CM5} = q_i^{Hirsh} + \sum_{j \neq i} T_{ij} B_{ij} \quad (8)$$

$$B_{ij} = \exp[-\alpha(r_{ij} - R_i - R_j)] \quad (9)$$

where  $r_{ij}$  is distance between atom  $i$  and  $j$ ,  $B_{ij}$  may be regarded as their Pauling bond order,  $R_i$  and  $R_j$  are their atomic covalent radii, which are defined as follows: For  $Z = 1-96$ , the average between CSD radii and Pyykkö radii are used, while for  $Z = 97-118$ , the Pyykkö radii are employed. The global parameter  $\alpha$  equals to  $2.474 \text{ \AA}^{-1}$ .

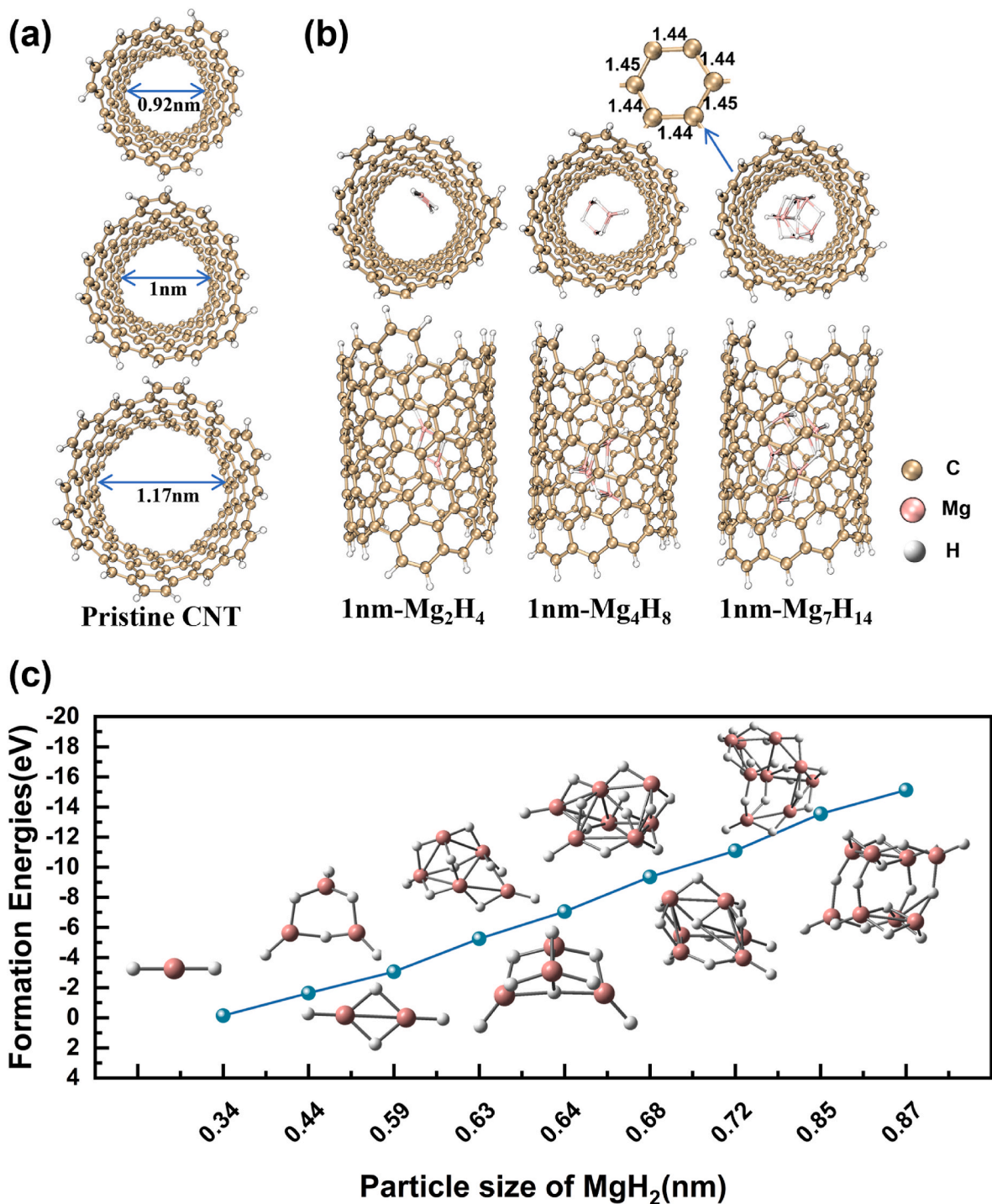


Fig. 1. (a) The structure of CNTs with pore sizes of 0.92 nm, 1 nm and 1.17 nm, (b) the structure of  $(MgH_2)_n$  clusters with a 1 nm pore size of CNTs nanoconfined to  $n = 2, 4, 7$ , and (c) the formation energy and structure of nanoclusters with different particle sizes  $(MgH_2)_n$  ( $n = 1-9$ ).

### 3. Results and discussion

#### 3.1. Model establishment

To elucidate the interaction between particle size and pore diameter in optimizing the dehydrogenation performance of  $\text{MgH}_2$  nanoparticle clusters encapsulated within CNTs, we have constructed CNTs with varying pore diameters, encompassing 0.92 nm CNTs (constructed with 142C atoms and 26H atoms appended on both ends to neutralize the negative charge), 1 nm CNTs (composed of 160C atoms and 28H atoms), and 1.17 nm CNTs (composed of 156C atoms and 36H atoms). Among the examined structures, the spin multiplicity is designated as 1 for the majority, with notable exceptions being the CNTs with pore sizes of 0.92 nm doped with 0.58 wt% B, 1 nm doped with 0.52 wt% B, and 1.17 nm doped with 0.58 wt% B, where the spin multiplicity is set to 2. Additionally, CNTs with B concentrations ranging from 0.29 to 1.18 wt% B for 0.92 nm CNTs, 0.26–1.04 wt% B for 1 nm CNTs, and 0.26–1.06 wt% B for 1.17 nm CNTs were synthesized by incorporating 1–4 B atoms, as depicted in Fig. 1a and b shows the optimal configuration of nanoparticle clusters such as  $\text{Mg}_2\text{H}_4$ ,  $\text{Mg}_4\text{H}_8$ ,  $\text{Mg}_7\text{H}_{14}$ , etc. (The graphics of other structures are displayed on Fig. S1, S2 and S3, Afterwards, the coordinates of the three structures in Fig. 1b were also displayed). The C–C bond length of one benzene ring of carbon nanotubes is shown

Fig. 1b (average C–C bond length of 1.44 Å), The Mg–H bond length of  $\text{MgH}_2$  clusters is in the range of 1.7–1.9 Å (Fig. 3c), and the Mayer level of Mg–H bonds is in the range of 0.2–1 (Fig. 4c) which is consistent with previous experimental and theoretical values, verifying the standardization of our carbon nanotube model [49].

To acquire  $\text{MgH}_2$  nanoparticles of diverse sizes and structures with minimal energy, we conducted optimization studies on the configurations of 200  $(\text{MgH}_2)_n$  ( $n = 1–9$ ) clusters. This optimization process allowed us to identify the local minima among the 200 possible configurations, and the sizes and formation energies of these clusters were subsequently calculated. The particle sizes of  $(\text{MgH}_2)_n$  ( $n = 1–9$ ) clusters were determined to be 0.343 nm, 0.439 nm, 0.513 nm, 0.594 nm, 0.630 nm, 0.641 nm, 0.675 nm, 0.716 nm, 0.847 nm, and 0.874 nm. As depicted in Fig. 1c, the formation energy of  $\text{MgH}_2$  exhibits an upward trend with increasing  $n$ , suggesting that under standard conditions,  $\text{MgH}_2$  prefers to aggregate into larger clusters. Moreover, the calculated Mg–H bond lengths in  $\text{MgH}_2$  clusters range from 1.7 to 1.9 Å [50,51], which is consistent with the cognitive understanding of  $\text{MgH}_2$  clusters. The literature summarizes that the absolute binding energy of  $\text{MgH}_2$  clusters with different carbon-based carriers obtained by previous researchers is in the range of approximately 0.1–6.9 eV, which is consistent with the calculations in this paper [52].

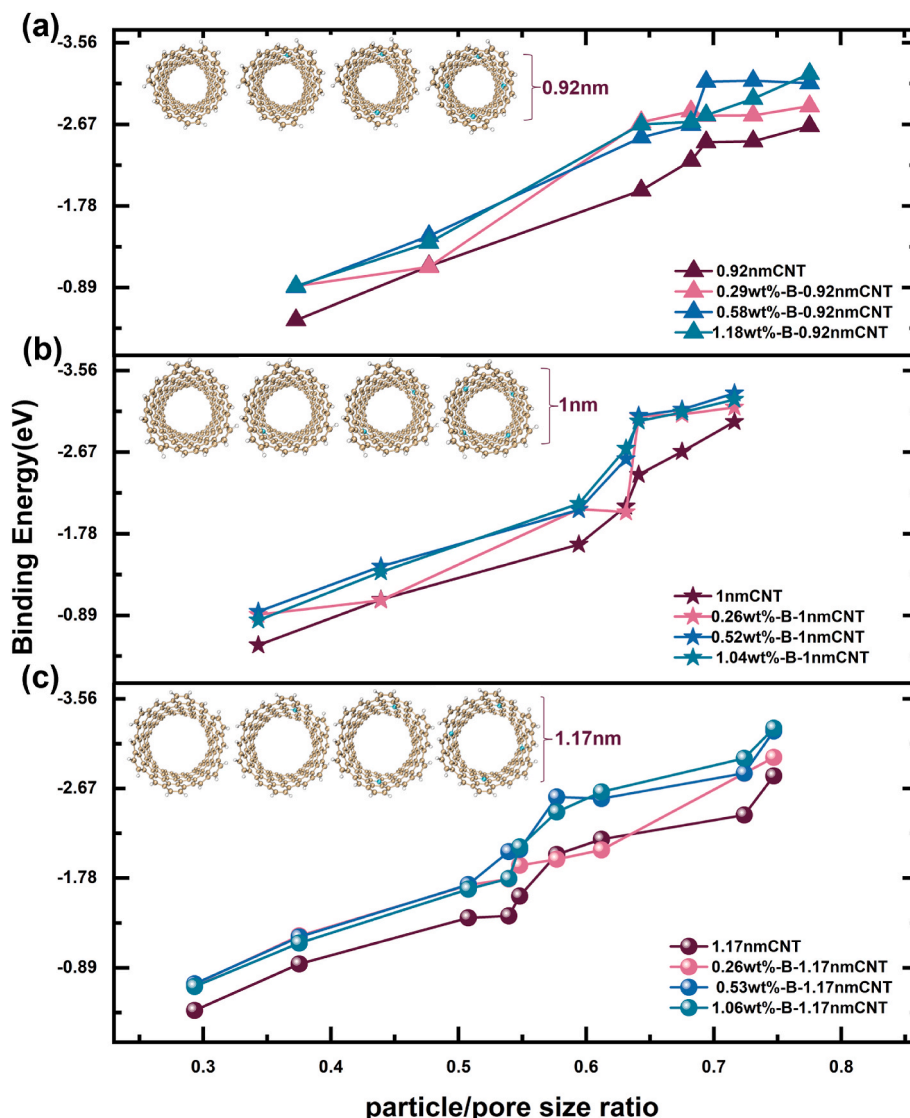


Fig. 2. The relationship between the ratio of  $\text{MgH}_2$  nanoparticle size to CNT pore diameter and the binding energy.

### 3.2. Structural stability

Utilizing the optimized structures aforementioned, the binding energy of CNT confined  $MgH_2$  clusters was calculated and depicted as the line graph in Fig. 2, plotted against the ratio of particle size to pore diameter. As shown in the figure, as the ratio of particle size to pore size increases, the binding energy of the nanoconfined structure also shows a monotonic trend. In the range of particle size to aperture ratio of 0.6–0.8, the best binding effect is found in the 1 nm CNTs nanoconfinement structure doped with 0.52 wt% B (Fig. 2b); In the range of particle size to aperture ratio of 0.2–0.6, the best binding effect is achieved through the nanoconfinement structure of 1.17 nm CNTs doped with 0.53 wt% B (Fig. 2c). The CNTs nanoconfined  $MgH_2$  structure has a negative binding energy as the particle size to pore size ratio of  $MgH_2$  to CNTs increases. As a result, the stability of the CNTs nanoconfined

structure system increases, and its cycling performance is also developing in a positive direction.

### 3.3. Mg–H bonding properties

On the basis of the above structure, the Mg–H bond lengths that meet the bonding conditions of each carbon nanotube confined  $(MgH_2)_n$  ( $n = 1-9$ ) cluster composite structure were statistically analyzed. The arithmetic mean of the Mg–H bond lengths in each composite structure was calculated, and the relationship between these values and the ratio of particle size to pore size was plotted as Fig. 3. The average bond length of Mg–H bonds in the structure of nanoconfined  $Mg_9H_{18}$  (i.e. a series of structures with the largest particle size to pore size ratio) is about 1.87 Å, making it the structure with the longest bond length. The shortest Mg–H bond length is 1.73 Å. This is very consistent with the experimentally

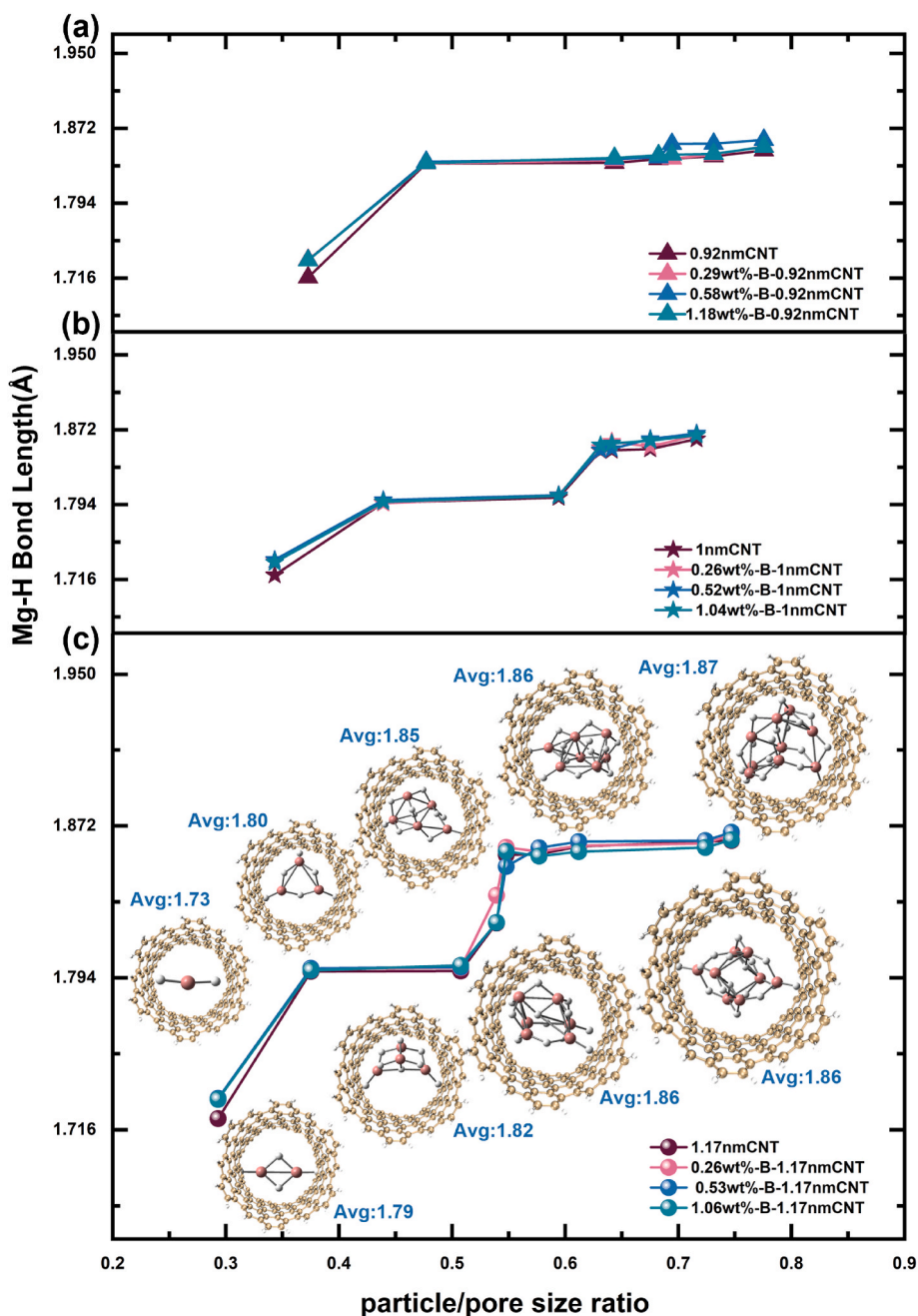


Fig. 3. The relationship between the ratio of  $MgH_2$  nanoparticle size to (a) 0.92 nm, (b) 1 nm, and (c) 1.17 nm CNT pore diameter and the average of all Mg–H bond lengths in  $MgH_2$  nanoparticles.

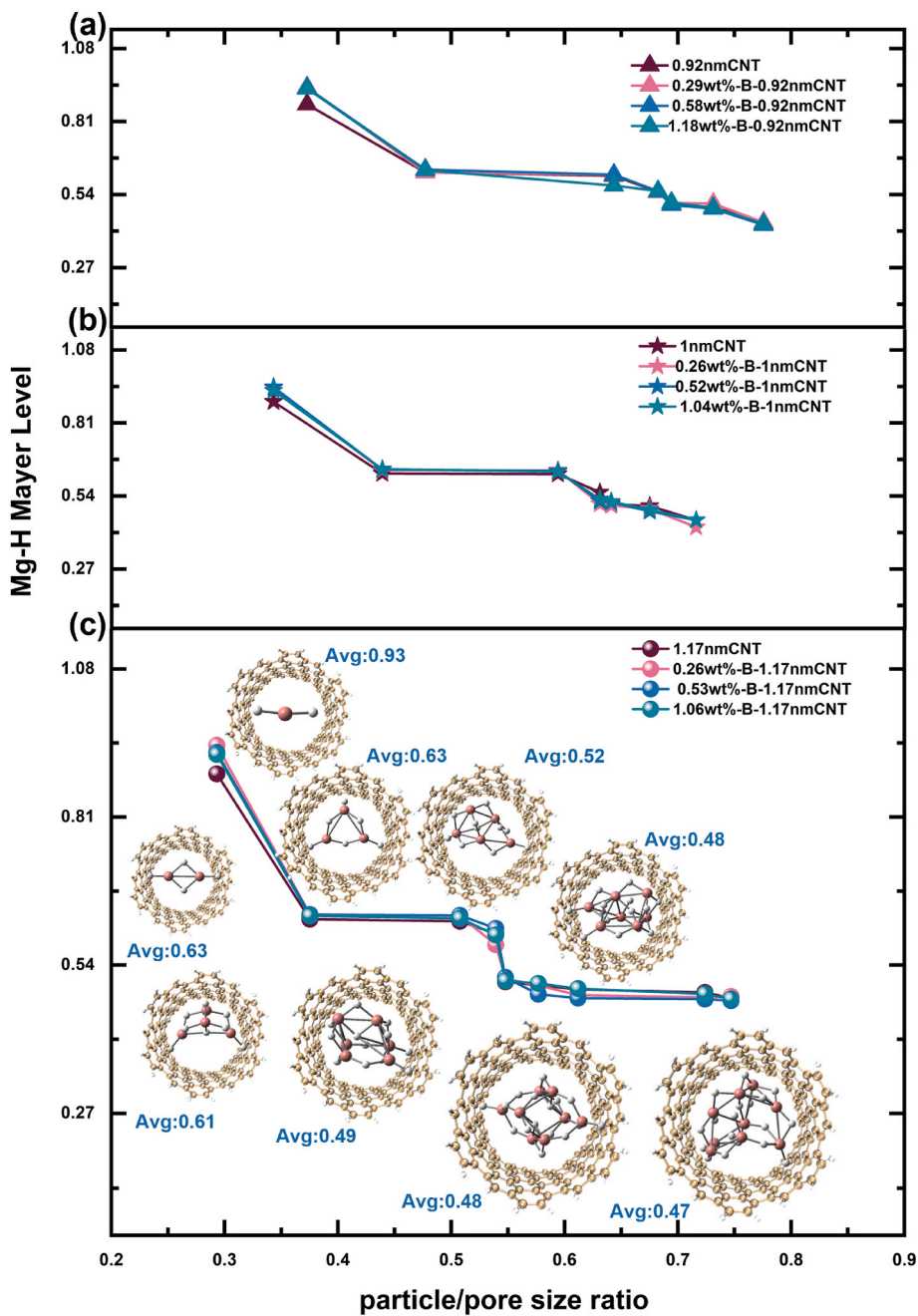


Fig. 4. Relationship between the ratio of MgH<sub>2</sub> nanoparticle size to CNT pore diameter and the average Mayer level of all Mg-H bonds in MgH<sub>2</sub> nanoparticles.

determined Mg-H bond length, thus verifying the accuracy of our calculation range [53,54]. The overall growth of the 0.92 nm nanoconfined structure and its structure doped with 0.29–1.18 wt%B was gentle after 0.47, with the growth trend of the 0.58 wt% B element doped nanoconfined structure significantly higher than other structures after a ratio of 0.7 (Fig. 3a); The 1 nm nanoconfined structure and the structure doped with 0.26–1.04 wt%B exhibit the same trend, with a plateau period of 0.44–0.6 and 0.63–0.8 in ratio (Fig. 3b); After a sharp increase, both the 1.17 nm nanoconfined structure and its doped B element structure entered a plateau period. After a gradual increase in particle size to aperture ratio of 0.37–0.5, the structure rapidly increased again and then slowly increased again after 0.55 (Fig. 3c). Overall, as the ratio of particle size to pore size increases, the average bond length of Mg-H bonds shows an upward trend.

In addition, we also calculated the Mayer bond order of all Mg-H bonds in the nanoconfined structure of MgH<sub>2</sub> nanoparticles. The Mg-H

Mayer level of the original/doped nanoconfined structure with a pore size of 0.92 nm is 0.35–0.5, and the decrease trend of particle size to pore size ratio is severe within the range of 0.2–0.53 and 0.5–0.9 (Fig. 4a); The Mg-H Mayer level with a pore size of 1 nm exhibits a significant decrease in particle size to pore size ratio within the ranges of 0.3–0.42 and 0.6–0.9 (Fig. 4b); The Mg-H Mayer level with a pore size of 0.92 nm exhibits a significant decrease in particle size to pore size ratios within the ranges of 0.2–0.35 and 0.5–0.55 (Fig. 4c). We also present the overall optimal distribution model of Mg-H Mayer level in the (MgH<sub>2</sub>)<sub>n</sub> (n = 1–9) series structure of CNTs with a pore size of 1.17 nm doped with 0.53 wt% B in the graph. It can be clearly observed that: Among all MgH<sub>2</sub> cluster structures, the Mg-H bonds situated on the outer perimeter of isolated clusters exhibit the highest Mayer level, with a value of 0.9; Compared to the Mg-H bonds far from the wall of CNTs, the Mg-H bonds closer to the wall of CNTs have smaller level.

As the particle size to aperture ratio increased in the range of

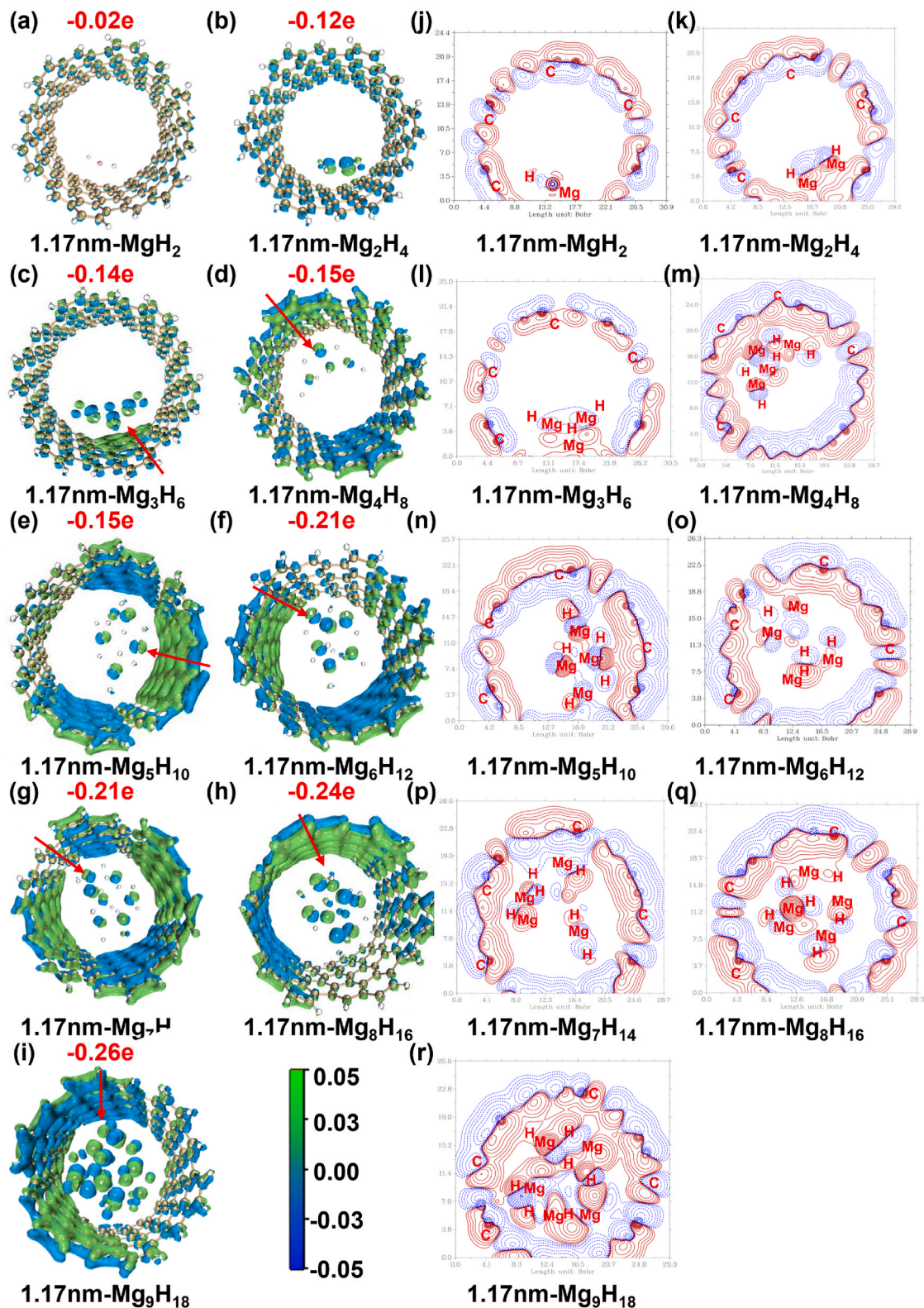


Fig. 5. (a–i) 3D and (j–r) 2D Charge Density Difference Maps and CM5 Charge Transfer Quantities of the Original 1.17 nm Pore Size CNT Confining (MgH<sub>2</sub>)<sub>n</sub> (n = 1–9) Structure (The isosurface size is ±0.05 electron/bohr<sup>3</sup>).

0.25–0.8, the Mayer level of Mg–H bonds gradually decreased, indicating a better weakening effect of Mg–H bonds. And the Mayer level of Mg–H bonds near the wall of CNTs is smaller, indicating that the wall of CNTs will play a certain catalytic role in promoting the separation of Mg–H bonds. In summary, with the increase of particle size to aperture ratio in the range of 0.25–0.8, the nanoconfinement of CNTs has a good promoting effect on the dehydrogenation kinetics of MgH<sub>2</sub> clusters.

### 3.4. Dehydrogenation temperature

All the results above and analyses are based on standard DFT calculations, which is incapable of describing the behavior of H<sub>2</sub> adsorption under practical operation condition (under elevated temperature and pressure). The adsorption and desorption behaviors of H<sub>2</sub> at the given temperature and pressure could be described by relative energy ( $E_r$ ) [55] defined as:

$$E_r = E(AB) - E(A) - nE(\text{Mg}) - n[E(\text{H}_2) + \mu_{\text{H}_2}(T, P)] \quad (10)$$

Among them,  $E(AB)$ ,  $E(A)$ ,  $E(\text{Mg})$ , and  $E(\text{H}_2)$  indicate the total energy of carbon confined MgH<sub>2</sub> system, carbon-based carrier, Mg and H<sub>2</sub> molecules.  $\mu_{\text{H}_2}(T, P)$  refers to the chemical potential of H<sub>2</sub> at the given temperature and pressure, which could be calculated by:

$$\mu_{\text{H}_2}(T, P) = \Delta H - T\Delta S + k_B T \ln \frac{P}{P_0} \quad (11)$$

where  $P_0$  represents the standard atmospheric pressure (0.1 MPa),  $k_B$  denotes the Boltzmann constant [55],  $H$  and  $S$  indicate the changes of enthalpy and entropy. Thermochemical tables are employed to obtain

the values of  $H - TS$  [56].

Fig. 6 shows the evolution of  $E_r$  as a temperature function on carbon nanotubes loaded with different (MgH<sub>2</sub>)<sub>n</sub> ( $n = 1, 3, 5, 7, 9$ ) clusters. According to this definition, negative  $E_r$  indicates that the adsorbed state of H<sub>2</sub> has more favorable energy than the desorbed state. At standard atmospheric pressure, the  $E_r$  values of all H<sub>2</sub> adsorption systems are negative within the temperature range of 0–390 K. However, as the temperature increases, the  $E_r$  values gradually approach zero, showing an enhanced desorption trend. At a pressure of 0.1 MPa, the critical temperature ( $T_c$ ) for H<sub>2</sub> desorption ranges approximately between 690 and 800 K. At 1 MPa, this critical temperature drops to approximately 400–430 K. Under otherwise constant conditions, as the pressure rises, the  $T_c$  for H<sub>2</sub> desorption decreases in all CNT confined MgH<sub>2</sub> cluster composite structures.

Finally, we have summarized the initial dehydrogenation temperatures of various carbon-based supports (CT carbon structure CT [31], carbon aerogel CA [28,29], Carbon nanotubes CNTs [57,58], graphene G [59]) confining MgH<sub>2</sub> nanoparticles under different ratios of MgH<sub>2</sub> particle size to pore diameter in previous studies. We conducted a comparative analysis with the Mayer bond orders of Mg–H bonds in (MgH<sub>2</sub>)<sub>n</sub> clusters nanoconfined in original 1.17 nm, 1 nm, and 0.92 nm CNTs (Fig. 7). As the ratio of particle size to pore diameter increases in the range of 0.1–0.8, both the Mayer level of Mg–H bonds and the initial dehydrogenation temperatures of MgH<sub>2</sub> nanoparticles nanoconfined in carbon-based supports decrease gradually, indicating our calculations are reliable. As the particle size to pore ratio of MgH<sub>2</sub> nanoparticles to CNTs increases, the weakening effect of Mg–H bonds becomes more pronounced, indicating that the increase in particle size to pore ratio enhances the dehydrogenation dynamic of MgH<sub>2</sub> nanoparticles.

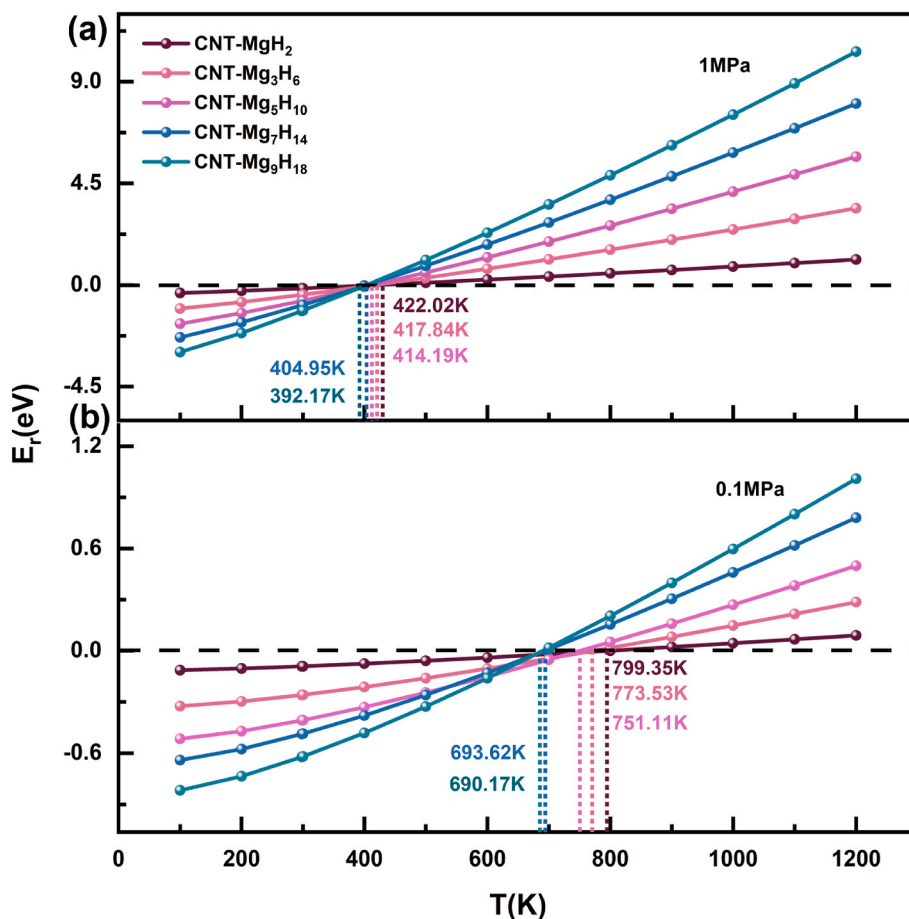
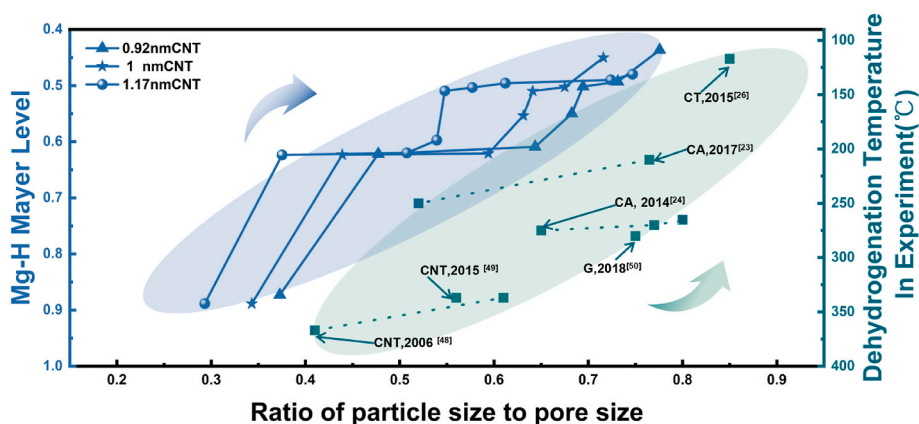


Fig. 6. The relative energy of (MgH<sub>2</sub>)<sub>n</sub> ( $n = 1, 3, 5, 7, 9$ ) under CNT confinement at (a) 1 MPa, (b) standard atmospheric pressure ( $P = 0.1$  MPa) varies with temperature.



**Fig. 7.** A comparison of the mayer level of Mg–H bonds in  $(\text{MgH}_2)_n$  clusters nanoconfined in original CNTs and the initial dehydrogenation temperatures of  $\text{MgH}_2$  nanoconfined in carbon-based supports in experiments, under the ratio of particle size to pore diameter.

### 3.5. The effect of B doping

B-doping introduces a modest enhancement in the Mg–H bond length of  $\text{MgH}_2$  confined within CNTs, albeit with limited overall impact, as several instances closely align along a common baseline (Fig. S13). Furthermore, the incorporation of B at varying concentrations exerts a specific influence on the binding energy, where nearly all B-doped nanoconfined structures exhibit a decrease in binding energy relative to pristine CNTs. Notably, the catalytic efficacy is most evident within a doping concentration range of 0.52–0.58 wt% B, as highlighted in Fig. S14.

In addition, B doping weakens the Mayer level of Mg–H bonds in  $\text{MgH}_2$  within carbon nanotubes. The nanoconfined structure doped with 0.53 wt% B demonstrates the optimal effect. The trend in the Mayer level of Mg–H bonds within the original and doped nanoconfined structures, featuring a 1 nm aperture, exhibits a more pronounced variation. Conversely, the Mayer level of Mg–H bonds in the original and doped nanoconfined structures with a pore size of 0.92 nm displays a smoother trend compared to the 1 nm series (Fig. S15).

### 3.6. Mechanism analysis

The dehydrogenation process of  $(\text{MgH}_2)_n$  ( $n = 1-9$ ) clusters nanoconfined within CNTs may involve a charge transfer mechanism. Therefore, we have calculated the Charge Model 5 (CM5) charges of  $(\text{MgH}_2)_n$  clusters nanoconfined in CNTs (Fig. 5). The 3D and 2D charge density difference maps were generated using Multiwfn [41] software, and the CM5 charge transfer amounts were computed accordingly. Fig. 5 depicts the charge density difference of  $(\text{MgH}_2)_n$  nanostructures nanoconfined within the original 1.17 nm pore size of CNTs. In these graphs, we observe a significant accumulation of charge density near the interface between  $(\text{MgH}_2)_n$  clusters and CNT walls. Simultaneously, the charge transfer process in the CNT nanoconfined  $(\text{MgH}_2)_n$  cluster structure is demonstrated, with electrons diffusing from the CNT to the interior of the  $(\text{MgH}_2)_n$  cluster. As the ratio of  $\text{MgH}_2$  to CNTs particle size increases, the CM5 charge density transfer of the structure also becomes increasingly negative.

Furthermore, a linear fitting analysis was conducted to examine the relationship between the CM5 charge transfer quantity and the Mayer bond order of Mg–H bonds in the nanoconfined  $\text{MgH}_2$  nanoparticles within CNTs with varying pore sizes and doped with different concentrations of boron (B) atoms. Specifically, for the nanoconfined structures of CNTs with original pore sizes of 1.17 nm, 1 nm, and 0.92 nm, the fitting result for the relationship between CM5 charge transfer quantity and Mayer bond order of Mg–H bonds is  $y = 1.61x + 0.88$ , with an  $R^2$  value of 0.88. However, for the B-doped CNT nanoconfined structures, the fitting result for the same relationship is  $y = 1.39x + 0.88$ , with a

reduced  $R^2$  value of 0.76 (Fig. 8a and b). Along the red line in the figure from top to bottom, it indicates an increase in the particle size to pore size ratio, the charge transfer of CM5 in the structure is becoming increasingly negative, and the Mayer level of Mg–H bonds is decreasing.

As the ratio of  $\text{MgH}_2$  particle size to CNTs pore size increases, the CM5 charge transfer of the structure also shows an increasingly negative trend. Compared with the relationship between particle size to aperture ratio and binding energy, Mg–H bond lengths, and Mg–H bond Mayer level mentioned earlier, we found similar trends, which proves the correctness of our conclusions. Furthermore, it was elucidated that as the ratio of particle size to pore size increases, the cycling stability, dehydrogenation kinetics, and degree of charge transfer of CNT nanoconfined  $\text{MgH}_2$  nanoparticles all increase. Linear fitting analysis revealed a strong correlation between the charge transfer amount of CM5 and the Mayer level of Mg–H bonds.

## 4. Conclusions

To elucidate the size-matching effect of carbon nanotubes confining  $\text{MgH}_2$  nanoparticles, we constructed three types of pristine/B-doped carbon nanotube models with different pore sizes and nine types of  $\text{MgH}_2$  clusters with different particle sizes based on experimental literatures. Through calculating the Mg–H bond lengths, binding energies, and Mayer level of Mg–H bonds in these series of nanoconfined structures, as the ratio of the particle size of  $\text{MgH}_2$  clusters to the pore size of carbon nanotubes increases in the range of 0.2–0.8, the Mg–H bond lengths become longer, and the binding energies and Mayer level of Mg–H bonds in the optimized structures become smaller. As the particle size to pore size ratio increases, the calculated dehydrogenation temperature decreases, and the dehydrogenation temperature can be further reduced by increasing the pressure. Meanwhile, we compared our findings with experimental literature and found that the Mayer bond order of Mg–H bonds was consistent with the initial dehydrogenation temperature at the experimental level. As the particle size to aperture ratio increases, the binding energy of the system becomes more and more negative, the weakening effect of Mg–H bond becomes more and more obvious, and the dehydrogenation kinetics may become better and better. It may be related to charge transfer, and subsequently studied the electronic structure of carbon nanotubes confining  $\text{MgH}_2$  clusters, including 3D and 2D electron density differences and charge model 5 charge transfer amounts. Further understanding of the effect of charge transfer on the dehydrogenation of carbon nanotube-nanoconfined  $\text{MgH}_2$  clusters also reveals a similar pattern: as the ratio of particle size to pore size increases, the charge transfer becomes more intensive. There is also a good linear correlation between the Charge Model 5 charge transfer amount of the structure and the Mayer level of Mg–H bonds. To our knowledge, this is the first time that the size-matching

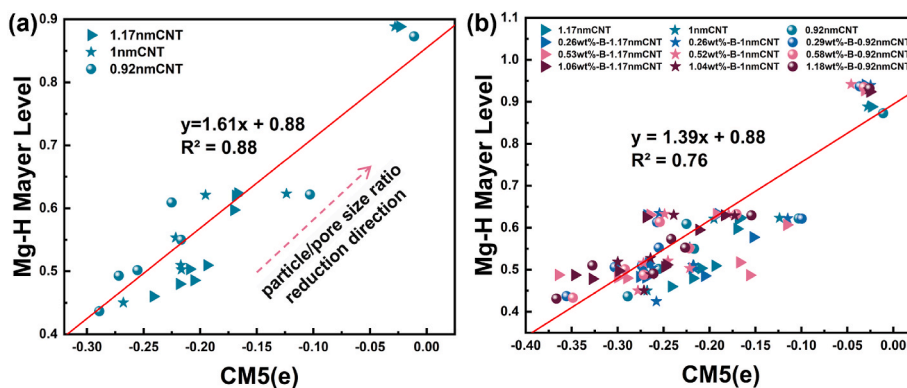


**Fig. 8.** The relationship between the CM5 charge transfer amount and the Mayer bond order of Mg–H bonds in MgH<sub>2</sub> nanostructures nanoconfined by different pore sizes of (a) pristine CNTs, (b) pristine CNTs with different pore sizes and doped with different concentrations of B atoms.

effect between carbon nanotubes and MgH<sub>2</sub> clusters has been summarized. This can help us deepen our understanding of the mechanism of carbon-based nanoconfinement of MgH<sub>2</sub> nanoparticles.

#### CRediT authorship contribution statement

**Lijun Fang:** Writing – review & editing, Conceptualization. **Chen Kai Liu:** Writing – original draft, Software, Formal analysis, Data curation, Conceptualization. **Yonghong Feng:** Data curation. **Zefan Gao:** Data curation. **Shilong Chen:** Data curation. **Mingye Huang:** Data curation. **Han Ge:** Data curation. **Linbin Huang:** Data curation, Methodology, Software. **Zhengyang Gao:** Writing – review & editing. **Weijie Yang:** Writing – review & editing, Methodology, Data curation.

#### Declaration of interests

Data are available upon request from the authors.

#### Acknowledgments

This work was funded by the Natural Science Foundation of Hebei (E2020502023).

#### Appendix A. Supplementary data

Supplementary data to this article can be found online at <https://doi.org/10.1016/j.ijhydene.2024.11.233>.

#### References

- Allendorf MD, Stavila V, Snider JL, et al. Challenges to developing materials for the transport and storage of hydrogen. *Nat Chem* 2022;14(11):1214–23. <https://doi.org/10.1038/s41557-022-01056-2>.
- Zhang S, Lee LH, Sun Y, et al. Materials for hydrogen mobile storage applications [C]. *IOP Conf Ser Earth Environ Sci* 2021;632(5):052087. <https://doi.org/10.1088/1755-1315/632/5/052087>. IOP Publishing.
- Ball M, Wietschel M. The future of hydrogen-opportunities and challenges. *Int J Hydrogen Energy* 2009;34(2):615–27. <https://doi.org/10.1016/j.ijhydene.2008.11.014>.
- Yanran W, Xiaowei C, Hongyu Z, Guanglin X, Dalin S, Xuebin Y. Heterostructures built in metal hydrides for advanced hydrogen storage reversibility. *Adv Mater* 2020;32:2002647. <https://doi.org/10.1002/adma.202002647>.
- Xiaoyue Z, Yahui S, Shunlong J, Jikai Y, Xuechun H, Wei C, Long Y, Guanglin X, Fang F, Dalin S, Xuebin Y. Solar-Driven reversible hydrogen storage. *Adv Mater* 2023;35:2206946. <https://doi.org/10.1002/adma.202206946>.
- Luo Y, Sun L, Xu F, et al. Improved hydrogen storage of LiBH<sub>4</sub> and NH<sub>3</sub>BH<sub>3</sub> by catalysts. *J Mater Chem A* 2018;6(17):7293–309.
- Lai Q, Paskevicius M, Sheppard DA, et al. Hydrogen storage materials for mobile and stationary applications: current state of the art. *ChemSusChem* 2015;8(17):2789–825. <https://doi.org/10.1002/cssc.201500231>.
- Zou Y, Xiang C, Qiu S, et al. Nanoconfined materials for hydrogen storage. *Prog Chem* 2013;25(1):115. <https://doi.org/10.7536/PC120615>.
- Pang Y, Liu Y, Gao M, et al. A mechanical-force-driven physical vapour deposition approach to fabricating complex hydride nanostructures. *Nat Commun* 2014;5(1):3519. <https://doi.org/10.1038/ncomms4519>.
- Niaz S, Manzoor T, Pandith AH. Hydrogen storage: materials, methods and perspectives. *Renew Sustain Energy Rev* 2015;50:457–69. <https://doi.org/10.1016/j.rser.2015.05.011>.
- Pukazhselvan D, Kumar V, Singh SK. High capacity hydrogen storage: basic aspects, new developments and milestones. *Nano Energy* 2012;1(4):566–89. <https://doi.org/10.1016/j.nanoen.2012.05.004>.
- Dong S, Liu H, Liu X, et al. Facile dehydrogenation of MgH<sub>2</sub> enabled by γ-graphyne based single-atom catalyst. *J Energy Storage* 2023;74:109484. <https://doi.org/10.1016/j.est.2023.109484>.
- Zhang X, Ju S, Li C, et al. Atomic reconstruction for realizing stable solar-driven reversible hydrogen storage of magnesium hydride. *Nat Commun* 2024;15(1):2815. <https://doi.org/10.1038/s41467-024-47077-y>.
- Dong S, Li C, Wang J, et al. The “burst effect” of hydrogen desorption in MgH<sub>2</sub> dehydrogenation. *J Mater Chem A* 2022;10(42):22363–72. <https://doi.org/10.1039/D2TA06458H>.
- Zhang X, Liu Y, Ren Z, et al. Realizing 6.7 wt% reversible storage of hydrogen at ambient temperature with non-confined ultrafine magnesium hydrides. *Energy Environ Sci* 2021;14(4):2302–13. <https://doi.org/10.1039/D0EE03160G>.
- Li W, Li C, Ma H, et al. Magnesium nanowires: enhanced kinetics for hydrogen absorption and desorption. *J Am Chem Soc* 2007;129(21):6710–1. <https://doi.org/10.1021/ja071323z>.
- Zhang XL, Liu YF, Zhang X, et al. Empowering hydrogen storage performance of MgH<sub>2</sub> by nanoengineering and nanocatalysis. *Materials Today Nano* 2020;9:100064. <https://doi.org/10.1016/j.mtnano.2019.100064>.
- Kim KC, Dai B, Johnson JK, et al. Assessing nanoparticle size effects on metal hydride thermodynamics using the Wulff construction. *Nanotechnology* 2009;20(20):204001. <https://doi.org/10.1088/0957-4484/20/20/204001>.
- Norberg NS, Arthur TS, Fredrick SJ, et al. Size-dependent hydrogen storage properties of Mg nanocrystals prepared from solution. *J Am Chem Soc* 2011;133(28):10679–81. <https://doi.org/10.1021/ja201791y>.
- Ibrahim KS. Carbon nanotubes? properties and applications: a review. *Carbon letters* 2013;14(3):131–44. <https://doi.org/10.5714/CL.2013.14.3.131>.
- Yang HB, Neal L, Flores EE, et al. Role and impact of surfactants in carbon nanotube dispersions and sorting. *J Surfactants Deterg* 2023;26(5):607–22. <https://doi.org/10.1002/jsde.12702>.
- Sui Y, Yuan Z, Zhou D, et al. Recent progress of nanotechnology in enhancing hydrogen storage performance of magnesium-based materials: a review. *Int J Hydrogen Energy* 2022;47(71):30546–66. <https://doi.org/10.1016/j.ijhydene.2022.06.310>.
- Peng J, He Y, Zhou C, et al. The carbon nanotubes-based materials and their applications for organic pollutant removal: a critical review. *Chin Chem Lett* 2021;32(5):1626–36. <https://doi.org/10.1016/j.ccl.2020.10.026>.
- Punetha VD, Rana S, Yoo HJ, et al. Functionalization of carbon nanomaterials for advanced polymer nanocomposites: a comparison study between CNT and graphene. *Prog Polym Sci* 2017;67:1–47. <https://doi.org/10.1016/j.progpolymsci.2016.12.010>.
- An KH, Lee YH. Electronic-structure engineering of carbon nanotubes. *Nano* 2006;1(2):115–38. <https://doi.org/10.1142/S1793292006000136>.
- Alapati SV, Johnson JK, Sholl DS. Identification of destabilized metal hydrides for hydrogen storage using first principles calculations. *J Phys Chem B* 2006;110(17):8769–76. <https://doi.org/10.1021/jp060482m>.
- Wu CZ, Wang P, Yao X, et al. Hydrogen storage properties of MgH<sub>2</sub>/SWNT composite prepared by ball milling. *J Alloys Compd* 2006;420(1–2):278–82. <https://doi.org/10.1016/j.jallcom.2005.10.028>.
- Huen P, Paskevicius M, Richter B, et al. Hydrogen storage stability of nanoconfined MgH<sub>2</sub> upon cycling. *Inorg* 2017;5(3):57. <https://doi.org/10.3390/inorganics5030057>.
- Au YS, Obbink MK, Srinivasan S, et al. The size dependence of hydrogen mobility and sorption kinetics for carbon-supported MgH<sub>2</sub> particles. *Adv Funct Mater* 2014;24(23):3604–11. <https://doi.org/10.1002/adfm.201304060>.

- [30] Jia Y, Sun C, Cheng L, et al. Destabilization of Mg–H bonding through nano-interfacial confinement by unsaturated carbon for hydrogen desorption from MgH<sub>2</sub>. *Phys Chem Chem Phys* 2013;15(16):5814–20. <https://doi.org/10.1039/C3CP50515D>.
- [31] Zlotea C, Oumellal Y, Hwang SJ, et al. Ultrasmall MgH<sub>2</sub> nanoparticles embedded in an ordered microporous carbon exhibiting rapid hydrogen sorption kinetics. *J Phys Chem C* 2015;119(32):18091–8. <https://doi.org/10.1021/acs.jpcc.5b05754>.
- [32] Zhang J, Xia G, Guo Z, et al. Synergetic effects toward catalysis and confinement of magnesium hydride on modified graphene: a first-principles study. *J Phys Chem C* 2017;121(34):18401–11. <https://doi.org/10.1021/acs.jpcc.7b05848>.
- [33] Xu Y, Zhou Y, Li Y, et al. Carbon-based materials for Mg-based solid-state hydrogen storage strategies. *Int J Hydrogen Energy* 2024;69:645–59. <https://doi.org/10.1016/j.ijhydene.2024.05.044>.
- [34] Liu M, Zhao S, Xiao X, et al. Novel 1D carbon nanotubes uniformly wrapped nanoscale MgH<sub>2</sub> for efficient hydrogen storage cycling performances with extreme high gravimetric and volumetric capacities. *Nano Energy* 2019;61:540–9. <https://doi.org/10.1016/j.nanoen.2019.04.094>.
- [35] Neese F, Wennmohs F, Becker U, et al. The ORCA quantum chemistry program package. *J Chem Phys* 2020;152(22). <https://doi.org/10.1063/5.0004608>.
- [36] Neese F. The ORCA program system. *Wiley Interdiscip Rev Comput Mol Sci* 2012;2(1):73–8. <https://doi.org/10.1002/wcms.81>.
- [37] Humphrey W, Dalke A, Schulten K. VMD: visual molecular dynamics. *J Mol Graph* 1996;14(1):33–8. [https://doi.org/10.1016/0263-7855\(96\)00018-5](https://doi.org/10.1016/0263-7855(96)00018-5).
- [38] Neese F, Wennmohs F, Hansen A, et al. Efficient, approximate and parallel Hartree–Fock and hybrid DFT calculations. A ‘chain-of-spheres’ algorithm for the Hartree–Fock exchange. *Chem Phys* 2009;356(1–3):98–109. <https://doi.org/10.1016/j.chemphys.2008.10.036>.
- [39] Hanwell MD, Curtis DE, Lonie DC, et al. Avogadro: an advanced semantic chemical editor, visualization, and analysis platform. *J Cheminf* 2012;4:1–17. <https://doi.org/10.1186/1758-2946-4-17>.
- [40] Meunier M, Robertson S. Materials studio 20th anniversary. *Mol Simulat* 2021;47(7):537–9. <https://doi.org/10.1080/08927022.2021.1892093>.
- [41] Tian L. Molclus Program, Version 1.9[J], <http://www.keinsci.com/research/molclus.html>.
- [42] Yang W, Xu S, Ma K, et al. Geometric structures, electronic characteristics, stabilities, catalytic activities, and descriptors of graphene-based single-atom catalysts. *Nano Mater Sci* 2020;2(2):120–31. <https://doi.org/10.1016/j.nanoms.2019.10.008>.
- [43] Fuster F, Grabowski SJ. Intramolecular hydrogen bonds: the QTAIM and ELF characteristics. *J Phys Chem* 2011;115(35):10078–86. <https://doi.org/10.1021/jp2056859>.
- [44] Rizhikov MR, Kozlova SG, Konchenko SN. Electron structure of iron chalcogenide clusters {Fe<sub>3</sub>Q} from AIM and ELF data: effect of hydrogen atoms on interatomic interactions. *J Phys Chem* 2009;113(2):474–9. <https://doi.org/10.1021/jp805941n>.
- [45] Lu T, Chen F. Multiwfn: a multifunctional wavefunction analyzer. *J Comput Chem* 2012;33(5):580–92. <https://doi.org/10.1002/jcc.22885>.
- [46] Mayer I. Charge, bond order and valence in the ab initio SCF theory. *Chem Phys Lett* 1985;117(4):396. [https://doi.org/10.1016/0009-2614\(83\)80005-0](https://doi.org/10.1016/0009-2614(83)80005-0).
- [47] Marenich AV, Jerome SV, Cramer CJ, et al. Charge model 5: an extension of Hirshfeld population analysis for the accurate description of molecular interactions in gaseous and condensed phases. *J Chem Theor Comput* 2012;8(2):527–41. <https://doi.org/10.1021/ct200866d>.
- [48] Hirshfeld FL. Bonded-atom fragments for describing molecular charge densities. *Theor Chim Acta* 1977;44:129–38. <https://doi.org/10.1007/BF00549096>.
- [49] Iijima S. Helical microtubules of graphitic carbon. *Nature* 1991;354(6348):56–8. <https://doi.org/10.1038/354056a0>.
- [50] Zhang J, Xia G, Guo Z, et al. Synergetic effects toward catalysis and confinement of magnesium hydride on modified graphene: a first-principles study. *J Phys Chem C* 2017;121(34):18401–11. <https://doi.org/10.1021/acs.jpcc.7b05848>.
- [51] Nielsen TK, Manickam K, Hirscher M, et al. Confinement of MgH<sub>2</sub> nanoclusters within nanoporous aerogel scaffold materials. *ACS Nano* 2009;3(11):3521–8. <https://doi.org/10.1021/nn901072w>.
- [52] Yan S, Wei L, Gong Y, et al. Enhanced hydrogen storage properties of magnesium hydride by multifunctional carbon-based materials: a review. *Int J Hydrogen Energy* 2023. <https://doi.org/10.1016/j.ijhydene.2023.11.219>.
- [53] Intemann J, Spielmann J, Sirsch P, et al. Well-defined molecular magnesium hydride clusters: relationship between size and hydrogen-elimination temperature. *Chem–Eur J* 2013;19(26):8478–89. <https://doi.org/10.1002/chem.201300684>.
- [54] Peng B, Li L, Ji W, et al. A quantum chemical study on magnesium (Mg)/magnesium–hydrogen (Mg–H) nanowires. *J Alloys Compd* 2009;484(1–2):308–13. <https://doi.org/10.1016/j.jallcom.2009.04.087>.
- [55] Wang J, Yong D, Lixian S. Ca-decorated novel boron sheet: a potential hydrogen storage medium. *Int J Hydrogen Energy* 2016;41(10):5276–83. <https://doi.org/10.1016/j.ijhydene.2016.01.039>.
- [56] Ma L, et al. First-principles study of hydrogen storage on Ca-decorated defective boron nitride nanosheets. *Phys E Low-dimens Syst Nanostruct* 2021;128:114588. <https://doi.org/10.1016/j.physe.2020.114588>.
- [57] Zhang Q, Huang Y, Ma T, et al. Facile synthesis of small MgH<sub>2</sub> nanoparticles confined in different carbon materials for hydrogen storage. *J Alloys Compd* 2020; 825:153953. <https://doi.org/10.1016/j.jallcom.2020.153953>.
- [58] Ullah Rather S, Taimoor AA, Muhammad A, et al. Kinetics of hydrogen adsorption on MgH<sub>2</sub>/CNT composite. *Mater Res Bull* 2016;77:23–8. <https://doi.org/10.1016/j.materresbull.2016.01.025>.
- [59] Wang K, Wu G, Cao H, et al. Improved reversible dehydrogenation properties of MgH<sub>2</sub> by the synergetic effects of graphene oxide-based porous carbon and TiCl<sub>3</sub>. *Int J Hydrogen Energy* 2018;43(15):7440–6. <https://doi.org/10.1016/j.ijhydene.2018.02.195>.